Characterization of Interfacial Structure in PEFCs: Water Storage and Contact Resistance Model

Tushar Swamy, E. C. Kumbur,[*,a,z] **and M. M. Mench**[**,z]

Fuel Cell Dynamics and Diagnostics Laboratory, Department of Mechanical and Nuclear Engineering, The Pennsylvania State University, University Park, Pennsylvania 16802, USA

In this work, an analytical model of the microporous layer (MPL) and the catalyst layer (CL) interface under compression is developed to investigate the effects of the MPL|CL interfacial morphology on the ohmic and mass transport losses at the MPL|CL interface in a polymer electrolyte fuel cell (PEFC). The model utilizes experimentally measured surface profile data as input. Results indicate that the uncompressed surface morphology of mating materials, the elasticity of PEFC components, and the local compression pressure are the key parameters that influence the characteristics of the MPL and CL contact. The model predicts that a 50% drop in the MPL and CL surface roughness may result in nearly a 40% drop in the MPL|CL contact resistance. The model also shows that the void space along the MPL|CL interface can potentially store a significant amount of liquid water (0.9–3.1 mg/cm^2), which could result in performance loss and reduced durability. A 50% drop in the MPL and CL surface roughness is expected to yield nearly a 50% drop in the water storage capacity of the MPL|CL interface. The results of this work provide key insights that will enhance our understanding regarding the complex relation between MPL|CL interfacial structure and cell performance.
© 2009 The Electrochemical Society. [DOI: 10.1149/1.3247585] All rights reserved.

Polymer electrolyte fuel cells (PEFCs) have tremendous potential as a power source for various applications. However, certain performance limitations have yet to be fully explained and optimized.[1] In particular, ohmic and mass transport losses can originate at the various interfaces that exist between the fuel cell components, including the microporous layer and the catalyst layer (MPL|CL) interface, the MPL and the diffusion media (MPL|DM) interface, and lastly, the DM and the bipolar plate (DM|BP) interface. Out of the existing interfaces, the MPL|CL interface carries especially high importance due to its direct influence on the electrode structure and performance. Because little is understood or yet published regarding the MPL|CL interfacial characteristics, major emphasis in this study was placed on understanding the role of the interfacial morphology, compression, and material properties on the MPL|CL interfacial region.

Due to the inherent roughness of the MPL and CL surfaces, the contact between the two materials under compression is imperfect (illustrated in Fig. 1), which results in a loss of contact area and the formation of interfacial gaps between these two surfaces. The improper contact not only gives rise to an electronic contact resistance (CR), but can also lead to liquid water pooling in the interfacial void space. This water pooling effect is important as it could play a pivotal role in blocking the reactant gas transport to the active sites in the CL, promoting mass transport losses. Therefore, it is necessary to investigate the impact of the MPL|CL interface to better understand water management.

There are many modeling studies in the literature that investigate the impact of the CL[2-11] and the MPL[12-21] on ohmic and mass transport losses in a PEFC; however, these studies do not consider a distinct MPL|CL interfacial region, instead they modeled the components using a separate set of control volumes. They apply numerical boundary conditions, such as flux and concentration matching, at the bordering control volumes in the two layers that form the interface. By preventing the independent treatment of the MPL|CL interface, the unique physical characteristics of the interfacial region are neglected. There exist a few experimental studies that have focused on interfacial losses,[22-27] however, only a couple of studies have dealt with the MPL|CL interface in particular.[26,27] Although a few numerical studies have attempted to incorporate the DM|CL interface (DM without MPL) into the modeling framework,[28,29] these

models neglect the geometry of the DM and CL surfaces; instead they consider a lumped/macro representation of the resulting interface. A few studies have attempted to model the DM|BP interfacial CR in a PEFC,[25,30-33] some of which take the average morphology of the mating surfaces into consideration as well.[25,32,33] However, to the best of the authors' knowledge, there is no study reported in the literature that utilizes the actual MPL|CL interface morphological structure to estimate the contact losses and associated performance drop due to the resulting imperfect contact.

Interfacial modeling has been extensively studied in the field of tribology and electrical contact mechanics.[34-41] These models are based on the Hertzian theory of contact and probabilistic modeling techniques to account for the stochastic nature of the mating surface profiles. Holm[34] studied the interaction of asperities on rough surfaces and pioneered the CR theory for a single contact between rough surfaces. Later, Greenwood and Williamson[35] (GW) presented an approach (GW model) where they extended Holm's work to span the entire mating area rather than focusing on a single contact point. However, one major drawback of the GW model is that it does not provide an approach to evaluate all of the input parameters for the contact model. Soon after, Nayak[36] presented a statistical approach to estimate these input parameters based on mating surface profile information. Because these models depend only on the surface profile characteristics and material properties, they can be extended to simulate the MPL|CL interfacial contact once reliable surface profile statistics are obtained.

This study is motivated by the need to gain a better understanding of the MPL|CL interfacial contact characteristics via considering the actual MPL and CL surface morphology and mating characteristics. The specific objective is to develop an analytical model that can predict the MPL|CL CR losses and the potential water accumulation capacity of the MPL|CL interface for different sets of materials under compression. The model is also capable of digitally reconstructing the MPL|CL interfacial morphology via control volume allocation, which can be incorporated into a macroscopic fuel cell model to facilitate a more accurate prediction of PEFC performance.

Method of Approach

The MPL|CL interface model presented herein requires three key input parameters, which are a function of the MPL and CL surface profile characteristics.[35] These parameters can be statistically evaluated if the discrete surface profile data of the two surfaces are known.[36] For this purpose, optical profilometry was used to obtain the MPL and CL surface profile data.[42] Detailed information regarding the optical profilometry measurements can be found in Ref. 42, however, for the sake of continuity, a brief description of the mea-
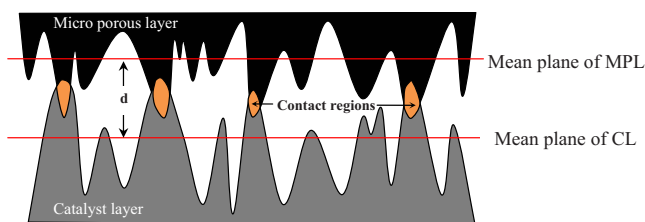
Figure 1. (Color online) Two-dimensional schematic of the MPL|CL interfacial contact.

Table I. Measured surface roughness data of MPL and CL samples. (Arithmetic mean values ± standard deviation of measurements.[42])

Sample	Average roughness, λ_a (μm)	rms roughness, λ_q (μm)	Crest–trough roughness, λ_t (μm)
MPL	5.35 ± 1.96	7.39 ± 3.20	68.32 ± 19.95
Cracked CL	2.19 ± 0.20	3.63 ± 0.21	26.56 ± 3.19

surement technique and the corresponding results are given below within the context of the interface model formulation presented in this study.

Experimental

The surfaces of the CLs from membrane electrode assemblies and the MPL of carbon paper type diffusion media (SGL 10BB) were investigated separately to generate the corresponding surface profile characteristics. Optical profilometry was used to quantify the surface roughness and morphology of these samples. The key advantage of this imaging technique is that it can perform high vertical resolution, quantitative and damage-free measurements of broad areas without any direct contact with the surface of interest. Details of this technique and measurement procedures are provided in Ref. 42. Before making measurements using optical profilometry, it is necessary to select an appropriate sampling interval to obtain accurate surface profile data.

A detailed analysis given in Ref. 41 discussed the issue concerning the choice of a suitable sampling interval required to accurately measure the roughness of a given surface. It was argued in Ref. 41 that a much larger value of the sampling interval compared to the root-mean-square (rms) roughness of the surface indicates excessive smoothening of the surface, which is undesirable. Furthermore, a much smaller value of the sampling interval relative to the rms roughness of the surface indicates that sufficient short-wavelength content is not filtered, resulting in sharp local peaks on the captured profile. This inclusion is unnecessary, because the plastic deformation of these localized peaks does not impact the overall characteristics of the elastic contact morphology.[41] Therefore, for relatively accurate surface roughness measurements, it was suggested that the measurement sampling interval should be proportional to the nominal rms roughness of the surface.[41] Contextually, for the MPL and CL samples tested in Ref. 42, the average rms roughness of the MPL and CL surfaces was determined to be 7.39 and 3.63 μm, respectively, via using a profiling instrument with a sampling interval of 0.82 μm in the x-direction and 0.95 μm in the y-direction along the surface.[42] These results indicate that the sampling interval of the profiling instrument and the roughness of the MPL and CL surfaces obtained are within an order of magnitude apart, suggesting a reasonably accurate and appropriate surface roughness measurement.

Measurements showed that both MPL and CL exhibit rough surface characteristics, having irregularities such as large valleys and deep cracks. However, the MPL surface is rougher in nature compared to the CL surface.[42] The difference between cracks or deep cuts in the CL and MPL surfaces should be distinguished from interfacial voids, which can occur as a result of surface roughness, regardless of the presence of cracks. It is important that the various surface characteristics of the sample be quantitatively distinguishable and isolated, therefore, surface profile information of a cracked CL can be obtained. The cracked CL consists of intentionally widened and/or deepened cracks, relative to the existing cracks on the regular CL. This exacerbation of crack width/depth may be accomplished either by accelerated coating of the CL slurry or by excessive heat-treatment to remove the volatile components in the slurry. The thickness of the MPL and CL was determined to be 80 and

30 μm, respectively. Table I lists the MPL and cracked CL surface roughness metrics that were measured for the tested samples via optical profilometry.

Model Formulation

The discrete surface data from optical profilometry measurements were first converted to a continuous representation, which was fed into the model to evaluate certain characteristic surface parameters of the MPL and the CL. These MPL and CL surface parameters were then combined to obtain the three key parameters required as input to the MPL|CL interface model. The model formulation was divided into the following steps: (*i*) surface profile characterization, (*ii*) contact model for smooth and rough surface, and (*iii*) contact model for two rough surfaces. These steps in the modeling procedure are explained in detail in the following sections.

Surface profile characterization.— To obtain the required interfacial morphology input parameters for the MPL|CL contact, a continuous mathematical representation of the discrete surface profile data of the two surfaces is necessary. For this purpose, the discrete Fourier transform (DFT) algorithm was utilized to represent the discrete measured data as a sum of sine and cosine series. Because the DFT algorithm is a commonly adopted procedure, details of the algorithm have been omitted from this text. A comprehensive description of the DFT algorithm can be found in Ref. 43. Representative cross sections of the measured MPL and CL discrete surface profile data were chosen from Ref. 42 and fed into the DFT algorithm as input. Consequently, continuous representations of the MPL and CL surface profiles, $Z_{MPL}(x)$ and $Z_{CL}(x)$, respectively, are obtained as output.

Contact model for smooth and rough surfaces.— Figure 2 represents the contact between a smooth surface and a single summit on a rough surface, showing the undeformed summit and its deformed shape when a load F is applied. To apply the GW model to the present case, the porosity of the contacting media at the MPL|CL interface was neglected, because the pore sizes were significantly less than the morphological features observed. Additionally, all
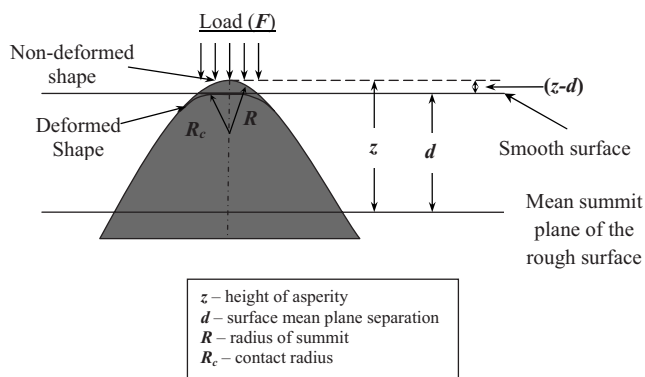

Figure 2. Contact geometry at a single summit on a rough surface with a smooth surface.

MPL|CL contacts were approximated to be elastic, and the contact points were largely separated so that the interaction between them can be neglected.

The MPL and CL surfaces are inherently rough with asperities distributed more or less randomly over the entire surface. According to the Hertzian theory of elastic contact,[35-38] the load F on a single summit (Fig. 2) of height z and radius R can be evaluated as

$$F = \frac{4}{3}E_{eq}R^{1/2}(z-d)^{3/2} \quad z > d \qquad [1]$$

and

$$E_{eq} = \left(\frac{1-v_1^2}{E_1} + \frac{1-v_2^2}{E_2}\right) \qquad [2]$$

where R is the radius of the summit before deformation, d is the surface mean plane separation, and v_i and E_i ($i = 1, 2$) are the Poisson's ratio and the Young's modulus of the two materials in contact, respectively. Equation 2 represents the effective Young's modulus as E_{eq}. By approximating the current flow across the interface to be independent due to the relatively large separation between asperities, one can define the electrical contact conductance for a single contact as[34]

$$g_c = \frac{4R_c}{\rho_1 + \rho_2} \qquad [3]$$

and

$$R_c = \sqrt{R(z-d)} \qquad [4]$$

where R_c is the deformed contact radius of the summit and ρ_i ($i = 1, 2$) is the electrical resistivity of the materials in contact, as shown in Fig. 2.

Because Eq. 1 and 3 were derived for a single asperity in contact, it is necessary to extend the theory to the entire surface encompassing all the asperities. As described, three key statistical parameters that characterize the rough surface must be evaluated and incorporated into Eq. 1 and 3, which are then integrated over the whole surface. The randomly distributed asperities on the given rough surface were approximated to be spherical in shape with a constant radius R and with a Gaussian probability distribution that can be defined as[35,37]

$$f(z) = \frac{1}{\sigma_{sum}\sqrt{2\pi}}e^{-z^2/2\sigma_{sum}^2} \qquad [5]$$

where σ_{sum} represents the standard deviation of summits. The probability θ that a randomly selected summit has a height in excess of the surface separation d can be expressed as

$$\theta(z > d) = \int_d^\infty f(z)dz \qquad [6]$$

It is clear that the load F is a function of the random variable z. The average value of a function of a random variable was obtained by integrating the product of the function and the probability density of the random variable over the domain of the random variable. Therefore, averaging the load F over the entire surface area and evaluating the compression pressure (CP) p by multiplying the resulting expression with the density of summits on the surface D_{sum} gives

$$p = \int_d^\infty \frac{4}{3}E_{eq}D_{sum}R^{1/2}(z-d)^{3/2}f(z)dz \qquad [7]$$

The average CP was approximated to be uniform over the MPL|CL contact interface being simulated. Similarly, integrating the electrical contact conductance in Eq. 3 over the entire contacting surface gives

Table II. Properties of various materials.

Properties	Material	Value	Units
Young's modulus[49]	DM	10,000	MPa
Electrical conductivity[50] (through plane)	MPL	300	S m^{-1}
Electrical conductivity[50] (through plane)	CL	200	S m^{-1}

$$g = \int_d^\infty \frac{4}{\rho_1 + \rho_2}D_{sum}R^{1/2}(z-d)^{1/2}f(z)dz \qquad [8]$$

Now, consider the normal probability distribution function $\varphi(x)$ which can be written as

$$\varphi(x) = \frac{1}{\sqrt{2\pi}}e^{-x^2/2} \qquad [9]$$

To simplify the integration in Eq. 7 and 8, the equations were written in terms of the normal probability distribution function $\varphi(x)$. Additionally, the height variables were scaled for numerical convenience using σ_{sum}. After some mathematical manipulation, the following equations were obtained

$$p = \frac{4}{3}E_{eq}D_{sum}R^{1/2}\sigma_{sum}^{3/2}F_{3/2}\left(\frac{d}{\sigma_s}\right) \qquad [10]$$

$$g = \frac{4}{\rho_1 + \rho_2}D_{sum}R^{1/2}\sigma_{sum}^{1/2}F_{1/2}\left(\frac{d}{\sigma_s}\right) \qquad [11]$$

$$r = \frac{1}{g} \qquad [12]$$

where r is the CR, and

$$F_n(t) = \int_t^\infty (x-t)^n\varphi(x)dx \qquad [13]$$

where the function in Eq. 13 is evaluated by expressing it in terms of the parabolic cylinder functions, $U(a,t)$,[44] as

$$F_n(t) = \frac{n!}{\sqrt{2\pi}}\frac{U\left(n+\frac{1}{2},t\right)}{e^{t^2/4}} \qquad [14]$$

It is clear from Eq. 10-12 that the CP p and the CR r are a function of the material properties (E_{eq} and ρ_i) and the three main statistical properties of the mating surfaces (D_{sum}, R, and σ_{sum}). The material (electrical) properties of the MPL and CL are given in Table II. To establish the choice of a suitable value of Young's modulus as an input to the model, attention must be diverted to the classic problem of bearing contact in tribology, to which the current model was originally applied.[35-38] In reality, it is known that no surface is perfectly clean. All material surfaces have a coating of particles (lubrication material, oxide material, dust, etc.), and therefore, there always exists a layer of finite thickness on the base material. Even though the Hertzian relations were derived for the materials in direct contact (the thin layer coatings), contact between bearing surfaces has been modeled using the current formulation with reasonable success, while neglecting the existence of the layer coatings. The key to this modeling triumph lies in the concept of relative dimensions, where it is argued that if the layer coating is relatively thin compared to the thickness of the bearing material, the bulk of the total deformation occurs in the bearing material. Therefore, the mechanical properties (Young's modulus) of the layer coating may have little impact on the mechanical contact characteristics (such as interfacial separation d) of the interface under load (although the electrical interfacial characteristics still depend on the layers in direct contact).

Drawing a parallel between the MPL/CL interfacial contact and the bearing contact, it was argued that the MPL/CL is relatively thin

compared to the DM. Therefore, as an approximation, the Young's modulus of the DM was chosen as an input to the model. The severity of the approximation depends on the relative dimensions and the relative Young's modulus of the DM when compared to the MPL/CL. Because the relative dimensions are known to be relatively small, attention must be focused on the relative Young's modulus of the DM. For a given compression pressure, a smaller Young's modulus of the DM, relative to that of the MPL|CL, would imply a much larger relative strain (which equates to a larger relative deformation) in the DM. Therefore, the approximation of selecting the Young's modulus of the DM as input may result in a smaller error if the Young's modulus of the DM is smaller relative to that of the MPL|CL.

As an added approximation, the Young's modulus of TGP-H-060 was used as model input (Table II), because the Young's modulus of SGL 10BB has not been reported in literature. Although the manufacturing process of the two DMs are different, both TGP-H-060 and SGL 10BB are carbon paper type DMs and essentially consist of a similar fused carbon fiber matrix.[b,c] Both DMs also have similar porosities (~0.8), contain a similar weight percentage of Teflon material (~5 % wt)[b,c] and therefore, it is argued that the Young's modulus of the two materials may lie within an order of magnitude apart. The error in the approximation depends on factors influencing the manufacturing process, such as heat-treatment. A parametric study on the Young's modulus of the DM was performed to determine its impact on the MPL|CL contact resistance.

Hereafter, because the material properties were chosen, the evaluation of these main statistical parameters (D_{sum}, R, and σ_{sum}) is necessary to solve the model equations. To evaluate these parameters, the following statistical manipulation was performed based on Ref. 36. Consider $Z(x)$, which is the continuous mathematical expression that represents the surface profile. At this juncture, the MPL and CL surfaces were approximated to be isotropic. The autocorrelation function (ACF), $A(x)$, is defined as.[36]

$$A(x) = \lim_{L \to \infty} \left\{ \frac{1}{2L}\left[\int_0^L Z(x)Z(x+j)dj \right] \right\} \quad [15]$$

where L is the length of the profile. The power spectral density function (PSDF), $\Phi(k)$, can be defined as the Fourier transform of the ACF as[36]

$$\phi(k) = \frac{1}{2\pi}\left[\int_{-\infty}^{\infty} A(x)e^{-2\pi i kx/N}dx \right] \quad [16]$$

where k is the set of wavenumbers of the spectral components that constitute the surface profile. The spectral moments, m_0, m_2, and m_4, of the PSDF are defined as[36]

$$m_i = \int_{-\infty}^{\infty} k^i \phi(k)dk \quad (i = 0, 2, 4) \quad [17]$$

The bandwidth parameter α, which depends on the shape and the extent of the spectrum of the roughness profile, is defined as[36]

$$\alpha = \frac{m_0 m_4}{(m_2)^2} \quad [18]$$

It was shown in Ref. 36 that the approximate values of the parameters R, σ_{sum}, and D_{sum} can be expressed solely as a function of the spectral moments (m_0, m_2, and m_4) and the bandwidth parameter α. The corresponding relations are shown below

$$R = \frac{3}{8}\left(\frac{\pi}{m_4}\right)^{1/2} \quad [19]$$

[b] SIGRACET GDL 10 series gas diffusion layer property sheet, SGL Technologies GmbH.
[c] Toray Carbon Fiber Paper "TGP-H" Property Sheet, Toray Industries, Inc. (2007).
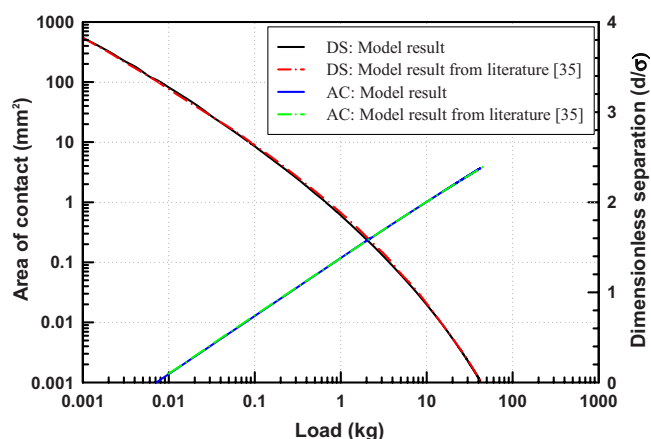

Figure 3. (Color online) Verification plot of area of contact (AC) and dimensionless separation (DS) vs the applied load (comparing current model results with the data reported in the literature[35]).

$$\sigma_{\text{sum}} = \left[\left(1 - \frac{0.8968}{\alpha}\right)m_0 \right]^{1/2} \quad [20]$$

$$D_{\text{sum}} = \frac{1}{6\pi\sqrt{3}}\left(\frac{m_4}{m_2}\right) \quad [21]$$

Contact model for two rough surfaces.— It has been shown that the contact of two rough surfaces is negligibly different from the contact of a smooth and an equivalent rough surface.[39,40] Hence, given the values of m_0, m_2, and m_4 of the two rough surfaces in consideration, i.e., the MPL and CL surfaces, the corresponding values for the equivalent rough surface can be computed in terms of their respective sums, i.e.

$$(m_0)_{\text{eq}} = (m_0)_{\text{MPL}} + (m_0)_{\text{CL}} \quad [22]$$

$$(m_2)_{\text{eq}} = (m_2)_{\text{MPL}} + (m_2)_{\text{CL}} \quad [23]$$

$$(m_4)_{\text{eq}} = (m_4)_{\text{MPL}} + (m_4)_{\text{CL}} \quad [24]$$

and the equivalent bandwidth parameter $(\alpha)_{\text{eq}}$ can be written as

$$(\alpha)_{\text{eq}} = \frac{(m_0)_{\text{eq}}(m_4)_{\text{eq}}}{(m_2)_{\text{eq}}^2} \quad [25]$$

Optical profilometry data from different locations on the MPL and CL samples were taken to ensure that the entire surface morphology was accurately captured.[42] The surface profile data corresponding to different cross sections of the MPL and CL surfaces were sequentially fed into the model as input. The equivalent values of m_0, m_2, m_4, and α were evaluated and substituted into Eq. 19-21 to obtain the statistical parameters R, σ_{sum}, and D_{sum}, which were averaged over numerous locations on the tested samples to cover the entire surface morphology. Using the equivalent surface parameters shown above, the rough–rough surface contact problem was solved using the equations for a smooth–rough surface contact derived in the previous section. Because the CP applied to the fuel cell was known, the surface separation d can be evaluated from Eq. 10. Knowing the surface separation d, the conductance g and, subsequently, the MPL|CL interfacial resistance r can be evaluated from Eq. 11 and 12, respectively.

Results and Discussion

Before conducting a parametric study of the MPL|CL interface, the variation of the area of contact and the dimensionless separation vs the applied load (Fig. 3) for a different contact problem given in Ref. 35 were simulated for verification. Figure 3 shows a comparison between the model results in the literature and the current model
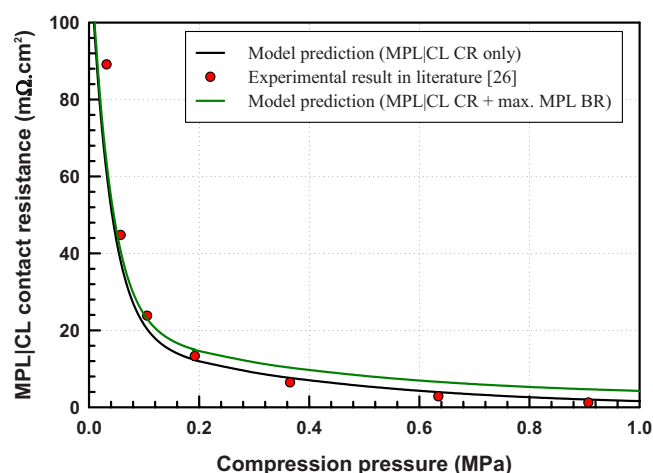
Figure 4. (Color online) Predicted MPL|CL CR vs applied CP. Model results for SGL 10BB (MPL|CL CR only and MPL|CL CR + maximum MPL BR) and experimental results for TGP-H-060 (with applied MPL) given in Ref. 26 are compared. The MPL on both materials have similar material properties and roughness values.[42,c] The DM material properties used are identical and equal to that of TGP-H-060.[49]

Figure 5. (Color online) A typical MPL|CL interface cross section.

predictions for the case given in Ref. 35. The results from the model in the literature and the current model show excellent agreement, indicating that the model developed in this study can successfully simulate the resulting contact interface between the two materials in consideration, as predicted by the model formulation.

Reverting back to the MPL|CL contact, Fig. 4 depicts the variation of the MPL|CL CR as a function of the applied CP in a PEFC. A comparison of the model prediction (via using actual measured cross sections of the MPL and CL surfaces) and experimental results reported in Ref. 26 is also presented in Fig. 4. Although the DM used for the numerical simulation and the experimental data are from different manufacturers (SGL 10BB for model predictions and TGP-H-060 for the experiments[26]), a comparison between the results is reasonably justified due to the following arguments:

1. The Young's modulus of TGP-H-060 is used as model input, which is also the DM used for the experiment. Therefore, the difference in the dependence of the simulation and the experimental results on the material property of the DM is eliminated.

2. SGL 10BB comes with a precoated MPL by the manufacturer, whereas TGP-H-060 was coated with an MPL for the purpose of the experiment. However, both materials have similar material properties as well as similar average roughness values of approximately 8 μm.[42,c]

The data in Ref. 26 consist of combined MPL|CL CR and bulk MPL resistance. Based on a basic ohm's law calculation, the maximum bulk resistance (BR) of the MPL (under no compression) is determined to be approximately 2.67 mΩ cm².[1] Therefore, to enable a better comparison between the experimental and modeling results, two simulation curves, one consisting of only the MPL|CL CR and the other consisting of MPL|CL CR and maximum bulk MPL resistance combined, are presented in Fig. 4. Figure 4 clearly shows that the model predictions and the experimental results are in good agreement, indicating that the MPL|CL CR is significantly high at low compression, which can exist under the channel. This observation can be attributed to the fact that, as the CP is reduced, a lower number of asperities located on the MPL and CL surfaces come into contact. The loss in contact points can impede the electron flow across the interface, thereby resulting in an increased MPL|CL electronic (and thermal) interfacial resistance.

Figure 5 shows the predicted MPL|CL interfacial structure under a homogeneous compression of 1.5 MPa (e.g., under a typical land).
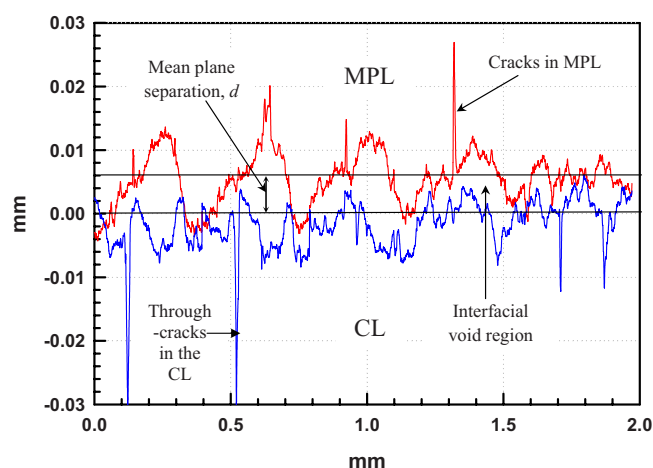
The cracks in the MPL and CL are clearly visible, and it was observed that some of the cracks in the CL penetrate into the entire layer.[42] Neglecting extremely deep cracks (profile height greater than 20 μm), the average peak-to-peak surface profile height for MPL and CL was 25 and 10 μm, respectively. The separation between mean planes, d, was determined to lie in the range of 5–10 μm. The maximum gap width was predicted to be close to 20 μm. It is evident from Fig. 5 that the MPL|CL interfacial gaps are relatively larger in dimension compared to the average pore size in the two layers, as reported in Ref. 1. This observation suggests that the MPL|CL interface could act as a locally low capillary pressure region to store liquid water in its voids, which could result in significant mass transport losses across the interface.

Figure 6 shows the variation of the predicted MPL|CL CR as a function of the applied CP for different degrees of uncompressed roughness (which is a function of the zeroth order spectral moment, m_0, of the PSDF of the surface profile) of the mating surface profiles. It can be seen from Fig. 6 that lowering the roughness of the MPL and CL surfaces by 50% (m_0 for the MPL and CL surfaces is lowered by 50% separately, and m_{eq} is generated from the resulting m_0 values of the two surfaces) results in nearly a 40% drop in the MPL|CL interfacial resistance. This significant drop in the CR can be attributed to the fact that as the roughness of the mating surfaces is decreased (i.e., smoother contact), the number of contact points increases, which, in turn, facilitates the electron flow across the
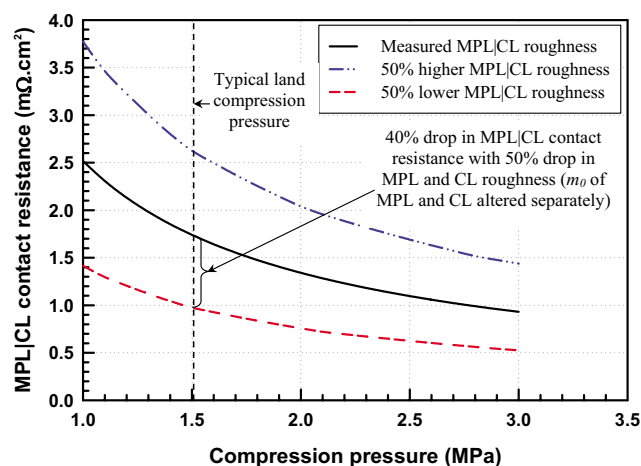

Figure 6. (Color online) Predicted MPL|CL CR vs CP for different degrees of MPL and CL roughness.
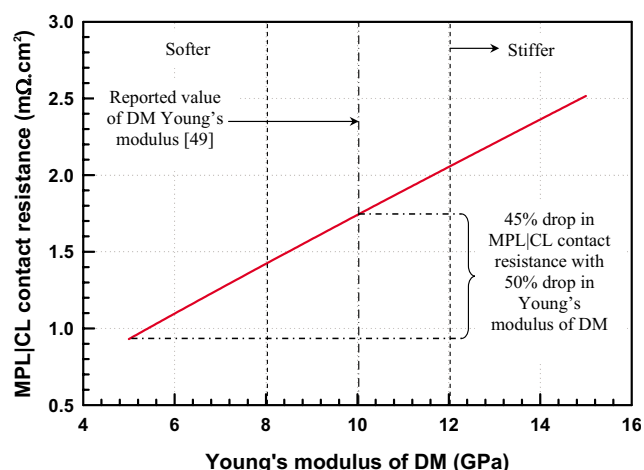
Figure 7. (Color online) Effect of the Young's modulus of the backing DM layer on the predicted MPL|CL CR for homogeneous CP of 1.5 MPa (under a typical land).

Figure 9. (Color online) Predicted MPL|CL CR as a function of the distance (x) under one set of land (L) and channel (C) affected due to inhomogeneous compression.

MPL|CL interface. Because the MPL surface exhibits a higher degree of roughness when compared to the CL tested,[42] the surface characteristics of the MPL is expected to dominate the interfacial region, and consequently, the MPL|CL CR.

Figure 7 shows the impact of the variation of Young's modulus of the backing DM layer on the MPL|CL CR for a homogeneous CP of 1.5 MPa, which is a typical compression value measured under the land. Young's modulus appears to have a significant impact on the MPL|CL interfacial resistance, because it is observed that a 50% drop in the Young's modulus of the DM yields approximately a 45% drop in CR. This strong dependence of the CR on the material property of the backing DM layer can be attributed to the fact that a drop in the Young's modulus of the DM results in the softening of the material, which allows the thin MPL and CL surfaces to exhibit a higher degree of conformation under compression. This provides flexibility to the MPL and CL surfaces, which greatly enhances the local mating percentage. As a result, a higher number of summits come into contact and a relatively lower MPL|CL CR is established. However, considering the channel, a stiffer material might be preferred, because it may sustain the land compression under the channel and avoid severe loss of contact under the channel.

Figure 8 shows the impact of the MPL summit density on the MPL|CL interfacial resistance. Figure 8 indicates that the MPL|CL CR drops by almost 10% with a 125% increase in the density of
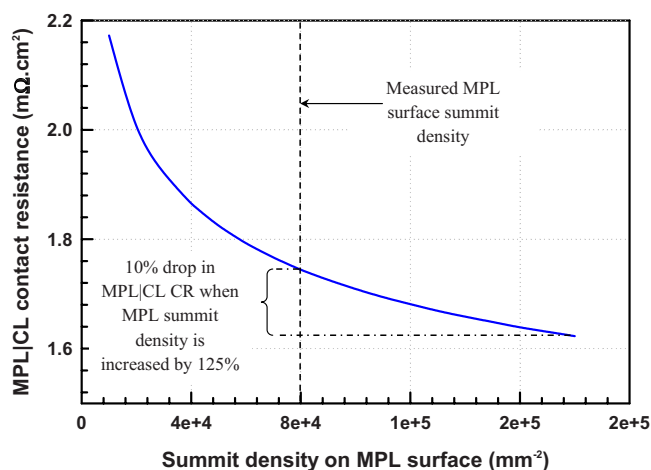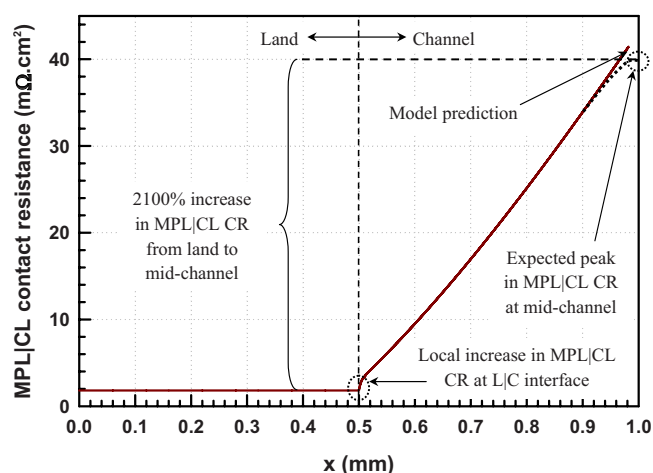

Figure 8. (Color online) Predicted MPL|CL CR vs the summit density on the MPL surface.

summits on the MPL surface. The reason for the observed drop in the MPL|CL CR can be attributed to the fact that an increase in the summit density implies a greater number of contact points, and consequently, an enhanced electron flow across the interface. An increase in the summit density may be achieved in practice by coating the MPL with a thin layer of highly conductive particles, much smaller in size relative to those that constitute the MPL structure. However, considering that the current size of particles that constitute the MPL is already very small (30–40 nm in the case of Vulcan XC-72 based MPLs), altering the surface summit density may not be as feasible and effective in reducing the MPL|CL CR losses as lowering the roughness of the mating surfaces.

Figure 9 shows the variation of the predicted MPL|CL CR under one set of land and channel configuration. To obtain the nonhomogeneous CP data required for the simulation, first, the DM thickness vs CP data given in Ref. 28 were used to evaluate the nonhomogeneous strain in the DM layer. Finally, using the DM strain data, the compression information under one land–channel configuration was extracted from the stress–strain data of the DM given in Ref. 25. The DM thickness measurement was performed ex situ for one set of land and channel (each of length 1 mm), and Fig. 9 shows the variation of the MPL|CL CR from midland to midchannel location with a span of 1 mm. The model predicts that there is approximately a 2100% increase in the MPL|CL CR at midchannel location as compared to CR under the land. This drastic increase can be attributed to the nonhomogeneous CP distribution. For instance, while moving into the channel and away from the land, the CP drops quite drastically and is minimal at midchannel position. To suppress this drastic increase in the MPL|CL CR, using a stiff DM may be a better option, because it could counteract the drop in the CP moving into the channel, maintaining better interfacial contact. It was mentioned earlier that a softer DM may be preferred under the land; however, considering the existence of competing Young's modulus effects under the land and the channel, the Young's modulus of the DM layer can be optimized to minimize the losses. Additionally, a relatively high value of MPL|CL CR at the land|channel interface was observed locally (Fig. 9), which can be attributed to the fact that there is a discontinuous transition from the land to the channel due to the straight edges of the land. This results in a local drop in the CP at the land|channel interface into the channel, yielding a high local MPL|CL CR. This effect could be negated by filleting the edges of the land to provide a less abrupt transition at the land|channel interface.

By utilizing the mean plane separation d (obtained as a model output) and the MPL|CL surface profile information, one can predict the capacity of potential water accumulation in the MPL|CL interfa-
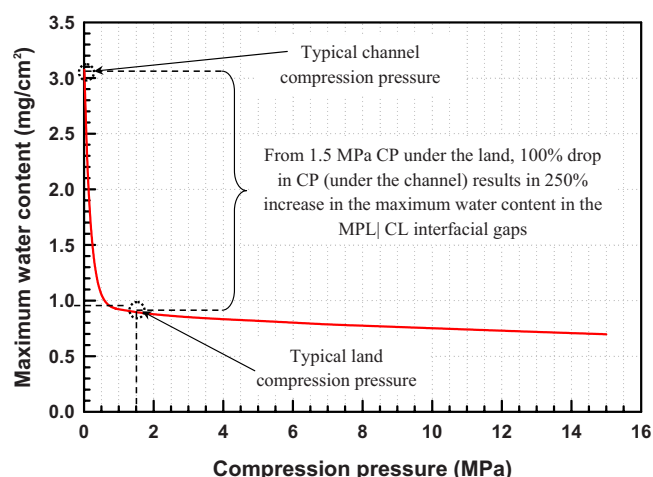
Figure 10. (Color online) Effect of the CP on the maximum water content in the MPL|CL interfacial gaps.

Figure 12. (Color online) Impact of the Young's modulus of DM on the maximum liquid water content in the MPL|CL interfacial gaps.

cial gaps. Knowledge of the maximum water content in the MPL|CL interface as a percentage of the total amount of water in a PEFC is critical, as it allows us to qualitatively estimate the impact of the MPL|CL interfacial voids on mass transport losses. Figure 10 shows the variation of the predicted maximum water content as a function of the applied CP in a PEFC. Figure 10 indicates that the MPL|CL interface can hold approximately 0.9–3.1 mg/cm^2 of liquid water when fully filled. The lower and upper limits of the prediction are at homogeneous CPs of 1.5 MPa (i.e., under the land condition) and 0.01 MPa ($\approx$0 MPa, i.e., under the channel condition), respectively. Neutron imaging results, reported in Ref. 45-47, suggest that nearly 5–15 mg/cm^2 of water can be stored in a PEFC under normal operating conditions. Therefore, considering the neutron imaging results and current model predictions, it is estimated that the MPL|CL interface can store nearly 6–18% of the total water content in the PEFC, which is significant considering the overall water balance in PEFCs. Cross-sectional X-ray radiography results[48] also indicate that the MPL|CL interface can store a considerable amount of liquid water (600 μm water thickness at 600 mA/cm^2) (Fig. 11), which is in good agreement with current predictions.

Several different scenarios were simulated via using the present model to determine the effects of compression on the water storage capacity at the MPL|CL interface. It was observed that an approximate 100% drop in the CP results in nearly a 250% increase in the
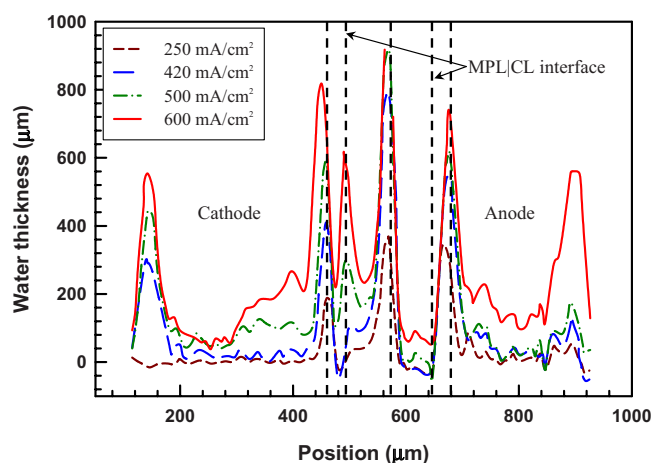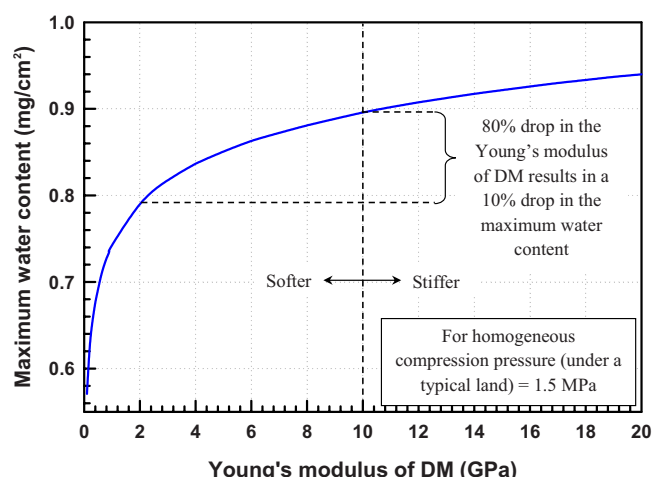
maximum water content in the MPL|CL interfacial gaps (Fig. 10). This suggests that the local CP in a fuel cell has a significant impact on the maximum potential water content that can be stored in the MPL|CL interface. It is not suggested here that the entire MPL|CL interfacial void volume is indeed normally filled with liquid water; instead, the present model predictions underline the existence of a significant potential storage location along the MPL|CL interface, which is worthy of investigation.

Figure 12 shows the effect of the variation in the Young's modulus of the backing DM layer on the maximum water content in the MPL|CL interface for an applied homogeneous CP of 1.5 MPa (i.e., under a typical land). The model predicts that an 80% drop in the Young's modulus of the DM from the currently selected value reported in Ref. 49 results in nearly a 10% drop in the maximum water content in the MPL|CL interfacial gaps. This indicates that a softer DM layer would perform better under the land. However, a stiffer DM layer may be preferred under the channel, as discussed.

Figure 13 shows the predicted impact of the MPL and CL surface roughness on the maximum water content in the MPL|CL interfacial gaps. It is estimated that a 50% drop in MPL and CL roughness (the same method used in Fig. 6 case is adopted here to achieve the drop in roughness) yields nearly a 50% drop in the maximum water content at a homogeneous CP of 1.5 MPa under the land, which is quite
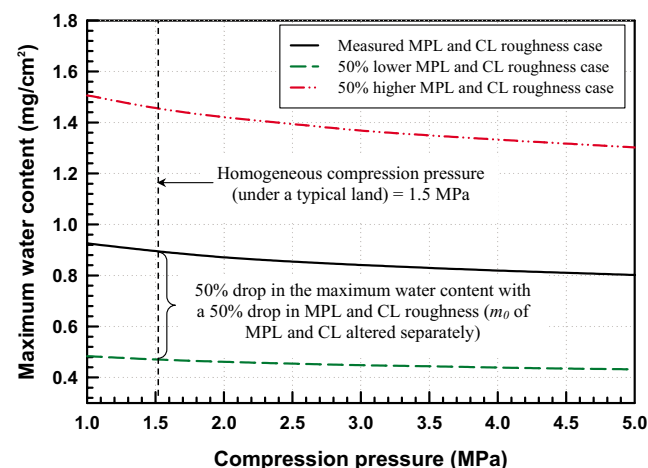

Figure 11. (Color online) Quantification and location of liquid water in a PEFC (figure adapted from Ref. 48).

Figure 13. (Color online) Effect of the variation in MPL and CL surface roughness on the maximum water content in the MPL|CL interfacial voids for a range of applied CPs.

significant. Based on this result and the analysis on the effect of MPL and CL roughness on the MPL|CL CR, it was observed that the MPL and CL roughness are expected to have a significant impact on the PEFC performance loss associated with the MPL|CL interface, which is currently under investigation in our laboratory.

Conclusions

An analytical model was developed to investigate the effect of the MPL and CL surface morphology and the applied CP on the ohmic and mass transport losses at the MPL|CL interface in a PEFC. Results show that the roughness of the mating surfaces and the elastic modulus of the backing DM layer have a significant impact on the polarization losses associated with the MPL|CL interface. The main conclusions are summarized below:

1. The MPL|CL interfacial gaps can be larger in size compared to the pores in the bulk PEFC layers. Thus, significant water pooling in the interfacial voids due to capillary flow could affect transport across the MPL|CL interface. The model suggests that the MPL|CL interfacial voids can hold approximately 6–18% of the total liquid water content in the PEFC, which is quite significant.

2. Due to the variation in the CP under the land and the channel, the MPL|CL CR is observed to be nearly 2100% higher in the middle of the channel compared to under the land for the materials simulated.

3. The model predicts a high value of local MPL|CL CR at the land|channel interface, which could be negated by rounding the edges of the land to provide a smoother transition at the land|channel interface.

4. For a homogeneous CP of 1.5 MPa (i.e., under a typical land), a 50% drop in the Young's modulus of the DM was predicted to yield a 45% drop in the MPL|CL interfacial resistance, and additionally, an 80% drop in the Young's modulus of the DM was found to result in nearly a 10% drop in the capacity of potential water accumulation in the MPL|CL interfacial gaps.

5. Results indicate that a softer DM layer would perform better under the land; however, a stiffer DM layer may be favored under the channel, as it can counteract the drop in the CP moving into the channel, maintaining better interfacial contact.

6. It is observed that a 50% drop in the MPL and CL surface roughness results in a 40% drop in the MPL|CL CR. Furthermore, a 50% drop in the MPL and CL surface roughness results in nearly a 50% drop in the capacity of potential water accumulation at the MPL|CL interfacial gaps.

The developed MPL|CL contact morphology model strengthens the understanding of the MPL|CL interfacial structure in a PEFC and the underlying physical processes that occur therein.

Acknowledgments

List of Symbols

d surface mean plane separation, mm
D density of summits on the surface, mm^{-2}
E_i Young's modulus, $(i = 1, 2)$ MPa
f Gaussian distribution
F compression load, kg
g conductance, $m\Omega^{-1} cm^{-2}$
j complex number, $\sqrt{-1}$
m_i spectral moment, $(i = 0, 2, 4)$ $mm^{(i-2)}$
p compression pressure, MPa

r resistance, $m\Omega\ cm^2$
R radius, mm
z height of asperity, mm
Z analytical representation of the surface profile data

Greek

α bandwidth parameter
θ probability
λ roughness, μm
ν_i Poisson's ratio, $i = 1, 2$
ρ_i resistivity, $(i = 1, 2)$ Ω mm
σ standard deviation, mm
φ normal distribution

Subscripts

eq   equivalent
c   contact (single)
sum   summit
a   average
q   root-mean-square
t   maximum height of the surface

References

1. M. M. Mench, *Fuel Cell Engines*, John Wiley & Sons, New York (2008).
2. V. Gurau, T. A. Zawodzinski, and J. A. Mann, *J. Fuel Cell Sci. Technol.*, **5**, 021009 (2008).
3. L. You and H. Liu, *Int. J. Heat Mass Transfer*, **45**, 2277 (2002).
4. C. Marr and X. Li, *J. Power Sources*, **77**, 17 (1999).
5. D. M. Bernardi and M. W. Verbrugge, *AIChE J.*, **37**, 1151 (1991).
6. T. E. Springer, M. S. Wilson, and S. Gottesfeld, *J. Electrochem. Soc.*, **140**, 3513 (1993).
7. R. Roshandel and B. Farhanieh, *Int. J. Hydrogen Energy*, **32**, 4424 (2007).
8. S. Kamarajugadda and S. Mazumder, *J. Power Sources*, **183**, 629 (2008).
9. L. You and H. Liu, *Int. J. Hydrogen Energy*, **26**, 991 (2001).
10. H. M. Yu, C. Ziegler, M. Oszcipok, M. Zobel, and C. Hebling, *Electrochim. Acta*, **51**, 1199 (2006).
11. P. K. Sinha, C. Y. Wang, and A. Su, *Int. J. Hydrogen Energy*, **32**, 886 (2007).
12. R. P. Ramasamy, E. C. Kumbur, M. M. Mench, W. Liu, D. Moore, and M. Murthy, *Int. J. Hydrogen Energy*, **33**, 3351 (2008).
13. W. M. Yan, C. Y. Hsueh, C. Y. Soong, F. Chen, C. H. Cheng, and S. C. Mei, *Int. J. Hydrogen Energy*, **32**, 4452 (2007).
14. J. H. Nam, K. J. Lee, G. S. Hwang, C. J. Kim, and M. Kaviany, *Int. J. Heat Mass Transfer*, **52**, 2779 (2009).
15. H. Meng, *Int. J. Hydrogen Energy*, **34**, 5488 (2009).
16. H. Nakajima, T. Konomi, and T. Kitahara, *J. Power Sources*, **171**, 457 (2007).
17. J. H. Nam and M. Kaviany, *Int. J. Heat Mass Transfer*, **46**, 4595 (2003).
18. U. Pasaogullari and C. Y. Wang, *Electrochim. Acta*, **49**, 4359 (2004).
19. A. Z. Weber and J. Newman, *J. Electrochem. Soc.*, **152**, A677 (2005).
20. Z. Qi and A. Kaufman, *J. Power Sources*, **109**, 38 (2002).
21. U. Pasaogullari, C. Y. Wang, and K. S. Chen, *J. Electrochem. Soc.*, **152**, A1574 (2005).
22. B. Avasarala and P. Haldar, *J. Power Sources*, **188**, 225 (2009).
23. I. Nitta, O. Himanen, and M. Mikkola, *Electrochem. Commun.*, **10**, 47 (2008).
24. I. Nitta, T. Hottinen, O. Himanen, and M. Mikkola, *J. Power Sources*, **171**, 26 (2007).
25. V. Mishra, F. Yang, and R. Pitchumani, *J. Fuel Cell Sci. Technol.*, **1**, 2 (2004).
26. J. Kleemann, F. Finsterwalder, and W. Tillmetz, *J. Power Sources*, **190**, 92 (2009).
27. R. Makharia, M. F. Mathias, and D. R. Baker, *J. Electrochem. Soc.*, **152**, A970 (2005).
28. T. Hottinen, O. Himanen, S. Karvonen, and I. Nitta, *J. Power Sources*, **171**, 113 (2007).
29. I. Nitta, S. Karvonen, O. Himanen, and M. Mikkola, *Fuel Cells*, **8**, 410 (2008).
30. X. Lai, D. Liu, L. Peng, and J. Ni, *J. Power Sources*, **182**, 153 (2008).
31. L. Zhang, Y. Liu, H. Song, S. Wang, Y. Zhou, and S. J. Hu, *J. Power Sources*, **162**, 1165 (2006).
32. Y. Zhou, G. Lin, A. J. Shih, and S. J. Hu, *J. Power Sources*, **163**, 777 (2007).
33. Z. Wu, S. Wang, L. Zhang, and S. J. Hu, *J. Power Sources*, **189**, 1066 (2009).
34. R. Holm, *Electrical Contacts Handbook*, Springer-Verlag, Berlin (1958).
35. J. A. Greenwood and J. W. P. Williamson, *Proc. R. Soc. London, Ser. A*, **295**, 300 (1966).
36. P. R. Nayak, *J. Lubr. Technol.*, **93**, 398 (1971).
37. J. I. McCool, *Wear*, **107**, 37 (1986).
38. J. A. Greenwood, *Wear*, **261**, 191 (2006).
39. A. W. Bush, R. D. Gibson, and T. R. Thomas, *Wear*, **35**, 87 (1975).
40. M. O'Callaghan and M. A. Cameron, *Wear*, **36**, 79 (1976).
41. L. Chang, *Proc. Inst. Mech. Eng., Part J: J. Eng. Tribol.*, **223**, 675 (2009).
42. F. E. Hizir, T. Swamy, S. O. Ural, E. C. Kumbur, and M. M. Mench, in *Proceedings of the Seventh International Conference on Fuel Cell Science Engineering and Technology*, ASME, p. 85092 (2009).
43. E. O. Brigham, *The Fast Fourier Transform*, Prentice-Hall, New York (2002).
44. M. Abramowitz and I. A. Stegun, *Handbook of Mathematical Functions*, Vol. 55, Applied Mathematics Series, U.S. Department of Commerce, Springfield, VA (1964).

45. A. Turhan, K. Heller, J. S. Brenizer, and M. M. Mench, *J. Power Sources*, **160**, 1195 (2006).
46. A. Turhan, K. Heller, J. S. Brenizer, and M. M. Mench, *J. Power Sources*, **180**, 773 (2008).
47. N. Pekula, K. Heller, P. A. Chuang, A. Turhan, M. M. Mench, J. S. Brenizer, and K. Ünlü, *Nucl. Instrum. Methods Phys. Res. A*, **542**, 134 (2005).

48. C. Hartnig, I. Manke, R. Kuhn, N. Kardjilov, J. Banhart, and W. Lehnert, *Appl. Phys. Lett.*, **92**, 134106 (2008).
49. A. Kusoglu, A. M. Karlsson, M. H. Santare, S. Cleghorn, and W. B. Johnson, *J. Power Sources*, **161**, 987 (2006).
50. S. Kim, M. Khandelwal, C. Chacko, and M. M. Mench, *J. Electrochem. Soc.*, **156**, B99 (2008).